Uncovering edge states and electrical inhomogeneity in MoS_2 field-effect transistors

Di Wu[a], Xiao Li[a], Lan Luan[a], Xiaoyu Wu[a], Wei Li[b], Maruthi N. Yogeesh[b], Rudresh Ghosh[b], Zhaodong Chu[a], Deji Akinwande[b], Qian Niu[a], and Keji Lai[a,1]

[a]Department of Physics, University of Texas at Austin, Austin, TX 78712; and [b]Microelectronics Research Center, University of Texas at Austin, Austin, TX 78758

Edited by Paul S. Weiss, University of California, Los Angeles, CA, and accepted by Editorial Board Member John A. Rogers June 20, 2016 (received for review April 15, 2016)

The understanding of various types of disorders in atomically thin transition metal dichalcogenides (TMDs), including dangling bonds at the edges, chalcogen deficiencies in the bulk, and charges in the substrate, is of fundamental importance for TMD applications in electronics and photonics. Because of the imperfections, electrons moving on these 2D crystals experience a spatially nonuniform Coulomb environment, whose effect on the charge transport has not been microscopically studied. Here, we report the mesoscopic conductance mapping in monolayer and few-layer MoS_2 field-effect transistors by microwave impedance microscopy (MIM). The spatial evolution of the insulator-to-metal transition is clearly resolved. Interestingly, as the transistors are gradually turned on, electrical conduction emerges initially at the edges before appearing in the bulk of MoS_2 flakes, which can be explained by our first-principles calculations. The results unambiguously confirm that the contribution of edge states to the channel conductance is significant under the threshold voltage but negligible once the bulk of the TMD device becomes conductive. Strong conductance inhomogeneity, which is associated with the fluctuations of disorder potential in the 2D sheets, is also observed in the MIM images, providing a guideline for future improvement of the device performance.

MoS_2 | microwave impedance microscopy | edge states | electrical inhomogeneity | metal-insulator transition

Electrostatic gating in the field-effect transistor (FET) configuration has played an essential role in the blooming field of semiconducting transition metal dichalcogenides (TMDs) such as MoS_2 and WSe_2 (1). The electrical control of carrier densities in these naturally formed 2D sheets is crucial for the realization of many intriguing phenomena, such as the metal–insulator transition (2–6), novel spin and valley physics (7–12), and superconducting phases (13–15). In addition, the carrier modulation provides an ideal tuning parameter to study the screening effect, which is particularly important for charge transport in 2D materials that are highly susceptible to local variations of the disorder potential (2–5, 16, 17). As a result, a complete understanding of the electronic properties of TMD FETs at all length scales, i.e., from local defects in the atomic scale, to electronic inhomogeneity in the mesoscale, to device performance in the macroscale, is imperative for both fundamental research on and practical applications of these fascinating materials.

Transport and most optical measurements on TMD FETs are inherently macroscopic in nature, in which the sample response is averaged over large areas. TMD films in actual devices, however, are far from electronically uniform. Due to the relatively large amount of intrinsic defects and the inevitable charged states in the substrates, mesoscopic electrical inhomogeneity is not uncommon in TMDs, leading to hopping transport and percolation transition in the devices (6, 16–19). Little is known, however, about the magnitude and characteristic length scale of such conductance fluctuations. For layered van der Waals materials, another unique feature occurs at the sample edges, where the broken crystalline symmetry and the presence of dangling bonds introduce additional electronic states to the bulk band structure. To date, edge states in TMDs are theoretically studied by first-principles calculations (20–22) and experimentally probed by scanning tunneling microscopy (STM) and spectroscopy (20, 23), whereas their contribution to the overall charge transport has not been fully addressed. Spatially resolved conductance maps are therefore highly desirable for the understanding of electrical inhomogeneity and edge channels in TMD FETs.

In this paper, we report the microwave impedance microscopy (MIM) (24, 25) study on the nanoscale conductance distribution during the normal operation of MoS_2 FETs. The experimental setup for our simultaneous transport and MIM measurements is schematically illustrated in Fig. 1*A*. The MoS_2 FETs and the MIM tip are mounted on the sample stage and the z scanner of a commercial atomic force microscope (AFM), respectively. During the contact-mode AFM scans, a low-power (~10 μW) 1-GHz microwave signal is delivered to the shielded cantilever tip (26) through the impedance match section. A dc bias can also be coupled to the tip using a bias tee. The reflected signal is then amplified and demodulated to form the MIM-Im and MIM-Re signals, which are proportional to the imaginary and real parts, respectively, of the small changes of tip–sample admittance in the measurement. Using the standard finite element analysis (FEA) modeling (24), the local sample conductivity can be mapped out with a spatial resolution determined by the tip diameter (on the order of 100 nm) rather than the free-space wavelength ($\lambda = 30$ cm) of the 1-GHz microwave. The conductance fluctuation in this

Significance

The performances of devices based on transition metal dichalcogenides (TMDs) are far from their intrinsic limits, presumably due to various disorders in these 2D crystals. To date, little is known about the magnitude and characteristic length scale of electrical inhomogeneity induced by the disorders in TMDs. In this paper, strong mesoscopic (submicrometer) electrical inhomogeneity in MoS_2 flakes, which reveals the potential fluctuations, was observed by a unique technique termed microwave impedance microscopy. The local conductance of edge states and its contribution to the transport were also resolved and analyzed experimentally for the first time, to our knowledge. The results provide a comprehensive understanding of the potential landscape in TMDs, which is very important for the improvement of device performance.

Author contributions: D.W. and K.L. designed research; D.W., X.L., L.L., X.W., W.L., M.N.Y., R.G., and K.L. performed research; D.W., X.L., L.L., X.W., W.L., M.N.Y., R.G., Z.C., D.A., Q.N., and K.L. analyzed data; and D.W. and K.L. wrote the paper.

The authors declare no conflict of interest.

This article is a PNAS Direct Submission. P.S.W. is a Guest Editor invited by the Editorial Board.

[1]To whom correspondence should be addressed. Email: kejilai@physics.utexas.edu.

This article contains supporting information online at www.pnas.org/lookup/suppl/doi:10.1073/pnas.1605982113/-/DCSupplemental.

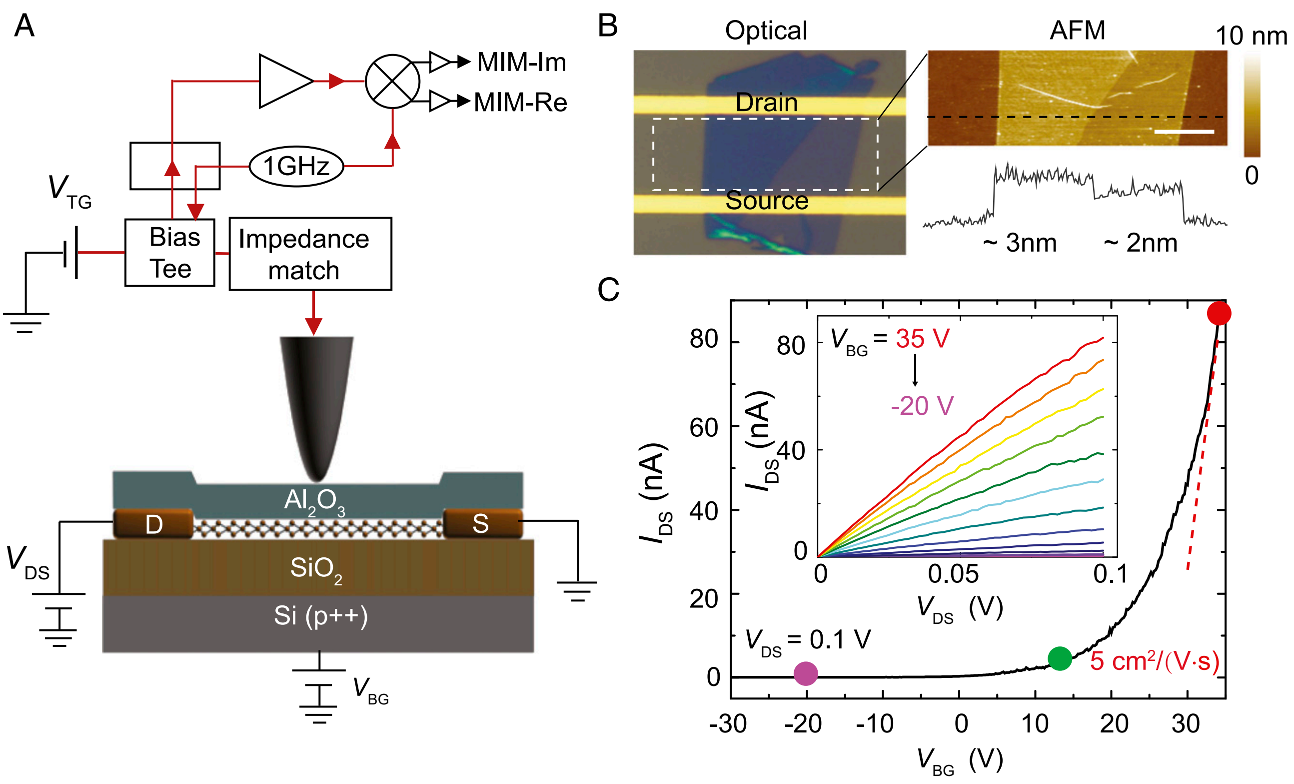

Fig. 1. Experimental setup and device characterization. (*A*) Schematic diagram of the device and the MIM setup. The 1-GHz microwave signal is guided to the tip through an impedance match section, and the reflected signal is detected by the MIM electronics. The carrier density can be either globally tuned by the back-gate voltage V_{BG} or locally modulated by the dc bias on the tip V_{TG}. (*B*) Optical and the zoom-in AFM images of an exfoliated MoS_2 FET device. (*Inset*) A line profile across the surface. (Scale bar, 5 μm.) (*C*) Transfer characteristics of the device at $V_{DS} = 0.1$ V. The dashed line is a linear fit to the curve for $V_{BG} > 30$ V, from which the field-effect mobility $\mu_{FE} \sim 5$ cm^2/(V·s) can be deduced. The solid circles (purple, green, and red) match the color coding in Fig. 5. (*Inset*) The output characteristics from $V_{BG} = 35$ V to −20 V with 5-V steps.

mesoscopic regime is particularly important for macroscopic device performance.

Results and Discussion

The starting materials of our FETs are few-layer exfoliated and monolayer (ML) chemical vapor deposited (CVD) MoS_2 flakes. The samples were transferred to or directly grown on SiO_2 (285 nm)/Si substrates, after which the source and drain contacts (20 nm Ag/30 nm Au) were formed via conventional electron beam (e beam) lithography and deposition (27, 28). To avoid direct contact between the metallic tip and the 2D sheets, which would strongly perturb the semiconducting MoS_2, we covered the device by the e-beam deposition of a thin (15 nm) layer of Al_2O_3. As a result, the carrier density in MoS_2 can be either globally modulated by the heavily doped Si back gate or locally tuned by the tip as a scanning top gate. Thanks to the capacitive tip–sample interaction, the MIM is capable of preforming subsurface electrical imaging (29–32) on the buried MoS_2 nanosheets.

Multiple exfoliated and CVD MoS_2 devices were investigated in this work, all of which exhibited similar behaviors. Fig. 1*B* shows the optical and the close-up AFM images of a typical FET fabricated on an exfoliated flake. The sample consists of two distinct regions with thicknesses of 2.1 nm and 2.8 nm, corresponding to three and four MLs, respectively, of MoS_2. Excluding several wrinkles from the exfoliation, the surface roughness of the sample is about 0.4 nm, presumably due to the fabrication process and Al_2O_3 deposition. The linear output characteristic I_{DS}–V_{DS} curves in Fig. 1*C*, *Inset* at different back-gate voltages (V_{BG}) are indicative of the good Ohmic contacts between Ag and MoS_2 (27). From the *n*-type transfer characteristics in Fig. 1*C*, the field effect mobility can be extracted by using the expression $\mu_{FE} = (dI_{DS}/dV_{BG}) \cdot (L/W) \cdot C_{ox}^{-1} \cdot V_{DS}^{-1} \approx 5\ \mathrm{cm}^2/(\mathrm{V.s})$, where C_{ox} is the parallel-plate capacitance of the SiO_2 layer, and L and W are the channel length and width, respectively. Note that, although the room temperature mobility is comparable to that of most back-gated devices reported in the literature (3, 5, 6, 16, 17), it is much lower than the theoretical phonon-limited value (33), suggesting the presence of considerable disorder in this device, which will be explored by the MIM study below.

Fig. 2*A* displays selected MIM images within the channel region of the device in Fig. 1*B* as a function of V_{BG}. The complete set of data and a video clip showing the gate dependence can be found in Fig. S1 and Movie S1, respectively. The evolution of local conductance maps vividly demonstrates the insulator-to-metal transition induced by the electrostatic field effect. When the flake is in the insulating limit at $V_{BG} = -30$ V, there is virtually no electrical contrast between MoS_2 and the substrate. As V_{BG} gradually goes up to 0 V, the contrast first emerges at the edges of the flake and then in the interior of the sample. Note that the MIM-Im signals are always higher on the four-ML region, with slightly smaller band gap (34) and higher mobility (35) than the three-ML part. For increasing V_{BG} toward 20 V, strong inhomogeneity is observed in both MIM output channels. At the same time, the MIM signals at the edges gradually merge into the bulk and become indistinguishable with the rest of the flake for $V_{BG} > 20$ V. For even higher back-gate voltages, the sample appears uniformly bright in MIM-Im and dim in MIM-Re. During the entire process, the MIM-Im signals on the MoS_2

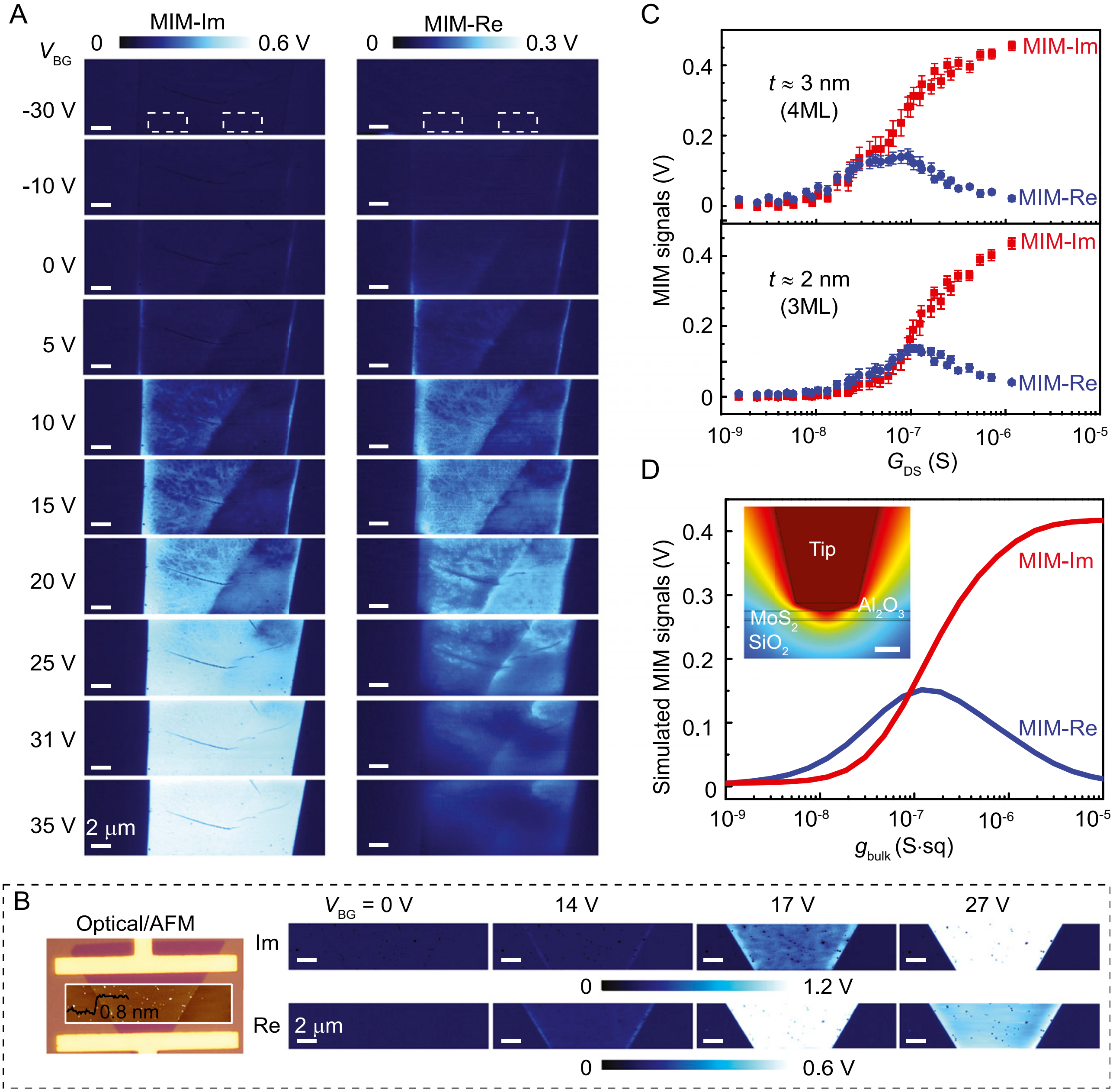

Fig. 2. Overall MIM response during the insulator-to-metal transition. (*A*) MIM-Im and MIM-Re images in the channel region (zoom-in image in Fig. 1*B*) of the device at selected back-gate voltages. (*B*) Optical, AFM (*Inset*), and MIM images of another FET device fabricated on a CVD-grown ML MoS_2 flake (see Fig. S3 for details). (*A* and *B* scale bars, 2 μm.) (*C*) Average MIM signals inside the white dashed boxes in *A* as a function of the source–drain conductance G_{DS}. (*D*) Simulated MIM signals as a function of the bulk sheet conductance g_{bulk}, showing very good agreement with the measured data in *C*. (*Inset*) The modeling geometry and the quasi-static potential distribution when the MoS_2 layer is insulating. (Scale bar, 50 nm.)

flake rise monotonically as increasing V_{BG}, whereas the MIM-Re signals reach a peak at V_{BG} ~20 V and diminish afterward. Similar MIM data are observed by gradually ramping up the dc tip bias V_{TG} during the scans, as shown in Fig. S2. The local gating, on the other hand, results in a complex in-plane potential gradient away from the tip (36) and therefore will not be analyzed in detail here. We emphasize that the same trend of MIM response has been seen in all six MoS_2 FETs in this study. Fig. 2*B* shows the optical, AFM, and MIM images of a CVD-grown ML MoS_2 device (complete set of data included in Fig. S3), with the overall behavior similar to that in Fig. 2*A*. In the following, we will focus on the exfoliated sample in Fig. 1 for quantitative analysis of the MIM data.

The average MIM-Im/Re signals within two 4 μm × 2 μm areas (white dashed boxes in Fig. 2*A*) on the four-ML and three-ML segments are shown in Fig. 2*C*, where the *x* axis is converted from V_{BG} to the two-terminal source–drain conductance (G_{DS}) by using the transfer curve in Fig. 1*C*. To quantitatively interpret the MIM signals as local conductance, we have calculated the MIM response curves as a function of the bulk MoS_2 sheet conductance g_{bulk} using FEA (24). Details of the FEA modeling and justification of the simulation parameters are included in Fig. S4. As shown in Fig. 2*D*, the simulated MIM-Im signal, which is proportional to the tip–sample capacitance, increases monotonically as increasing g_{bulk} and saturates at both the insulating ($g_{bulk} < 10^{-9}$ Siemens·sq or S·sq) and conducting ($g_{bulk} > 10^{-5}$ S·sq) limits. The MIM-Re signal, on the other hand, represents the effective loss in the tip–sample interaction and peaks at an intermediate g_{bulk} of $\sim 10^{-7}$ S·sq. Note that $G_{\mathrm{DS}} \approx g_{\mathrm{bulk}} \cdot W/L$ if the source/drain contact resistance is relatively small compared with the channel resistance. An excellent agreement between the experimental data and our modeling result can be obtained by comparing the averaged MIM signals in Fig. 2*C* and the simulation in Fig. 2*D*. The MIM images thus provide a quantitative measure of the mesoscopic conductance distribution in the MoS_2 FET.

A prominent feature in Fig. 2*A* is the emergence of conductive edge states before the bulk of the sample is populated by conduction electrons. The presence of localized edge channels on the boundary of a 2D system is one of the most intriguing phenomena in condensed matter physics (37). In the case of TMDs, both density functional theory (DFT) calculations (20–22) and STM measurements (20, 23) have revealed the metallic (semiconducting) states at the zigzag (armchair) edges, whereas their influence on the device performance has not been experimentally probed. The MIM-Im images on the three-ML side of the sample at selected V_{BG} are shown in Fig. 3*A*, with the line profiles across the sample edge (yellow dashed line) plotted in Fig. 3*B*. Note that the apparent width of ∼200–300 nm at different locations of the boundary is determined by the spatial resolution or the tip diameter d rather than the actual width w_{edge} of the edge states. To quantify the edge conductance, we performed 3D FEA modeling of the MIM response, in which a narrow conductive channel with $w_{\mathrm{edge}} = 5$ nm is situated in between the insulating substrate and the MoS_2 bulk. Because $w_{\mathrm{edge}} << d$, the simulation result is invariant with respect to the product of w_{edge} and the sheet conductance of the edge g_{edge}. Details and justifications of the modeling parameters are shown in Fig. S5. The edge and bulk conductance values determined by comparing the 3D FEA and the MIM data are plotted in Fig. 3*C*. As V_{BG} increases from −30 V to 0 V, g_{edge} rapidly increases for more than two orders of magnitude, whereas the bulk conductance g_{bulk} stays below our sensitivity limit of $\sim 10^{-9}$ S·sq. For 0 V < V_{BG} < 5 V, g_{edge} levels off and g_{bulk} starts to rise above the noise floor. For V_{BG} above 5 V, g_{edge} saturates around 4×10^{-5} S·sq, whereas g_{bulk} continues to increase as V_{BG} increases. The quantitative mapping of g_{edge} signifies the fundamental difference between the topologically trivial edge states in TMDs and the nontrivial quantum Hall (QH) (37) or quantum spin Hall (QSH) (38, 39) edges. The TMD edges in our case can be treated as a normal 1D conductor, where the carriers experience the usual scattering events. Given the FET channel length $L \approx 10$ μm in this sample, the maximum contribution of the edge states to the total conduction $G_{\mathrm{edge}} = g_{\mathrm{edge}} \cdot w_{\mathrm{edge}}/L$ is on the order of 10^{-8} S, which is negligible once the FET is turned on. The QH or QSH edge channels, on the other hand, are dissipationless due to the suppression of backscattering and are responsible for the transport quantization when the bulk is insulating. Indeed, in our previous MIM studies on both QH (30) and QSH (31) systems, the highly conductive edges display maximum MIM-Im and zero MIM-Re signals, in sharp contrast to the finite signals in both channels for the MoS_2 edges.

For further investigations of the observed edge states, we carried out first-principles DFT calculations (*Methods*) on one-ML and three-ML MoS_2 nanosheets. Fig. 4*A* shows the

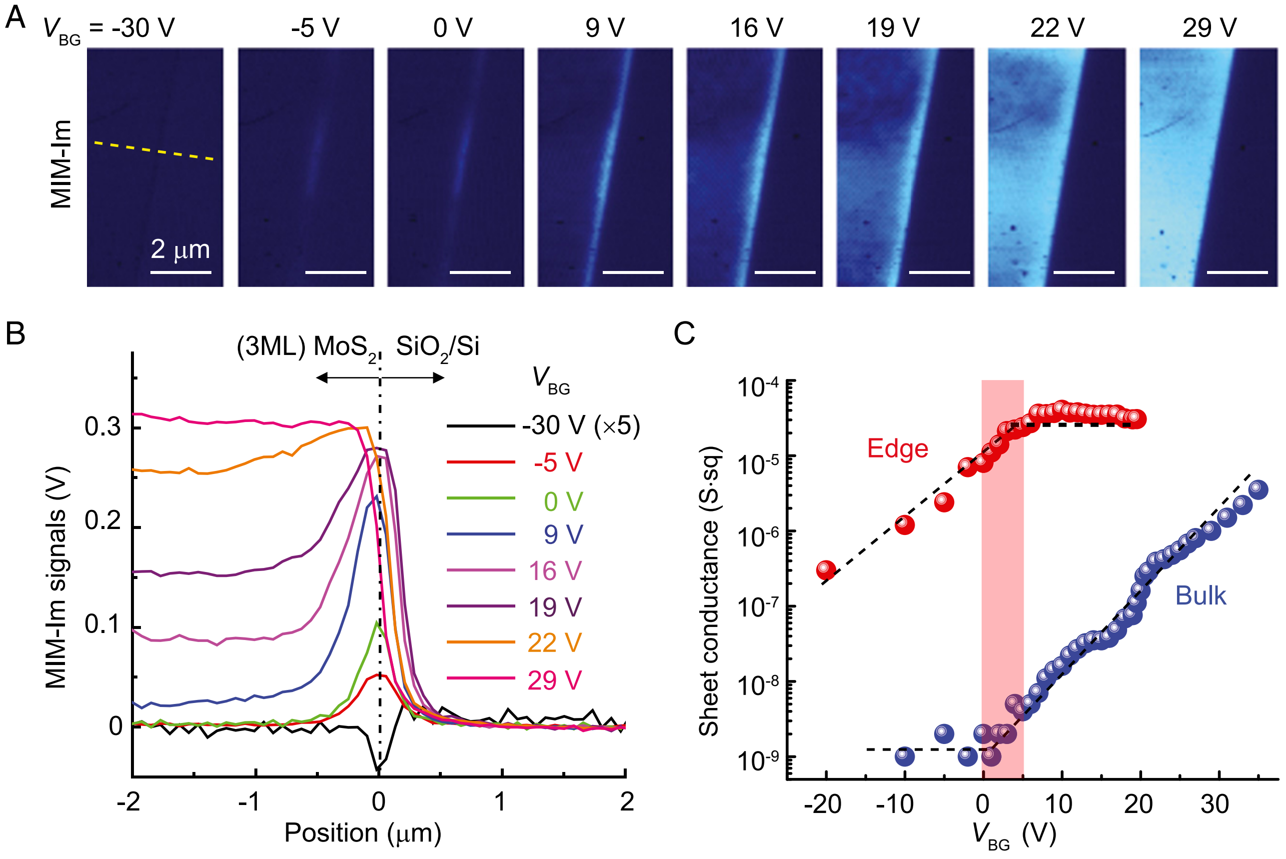

Fig. 3. Edge state conductance of MoS_2. (*A*) Selected MIM-Im images on the rightmost region of the flake. (Scale bars, 2 μm.) (*B*) Selected profiles (averaged over 20 lines) along the yellow dashed line in *A*. The physical boundary of the three-ML MoS_2 is centered in the plot. (*C*) Effective edge and bulk conductance as a function of V_{BG}. The shaded column marks the onset of bulk conduction and the saturation of edge conduction. The dashed lines are guides to the eyes.

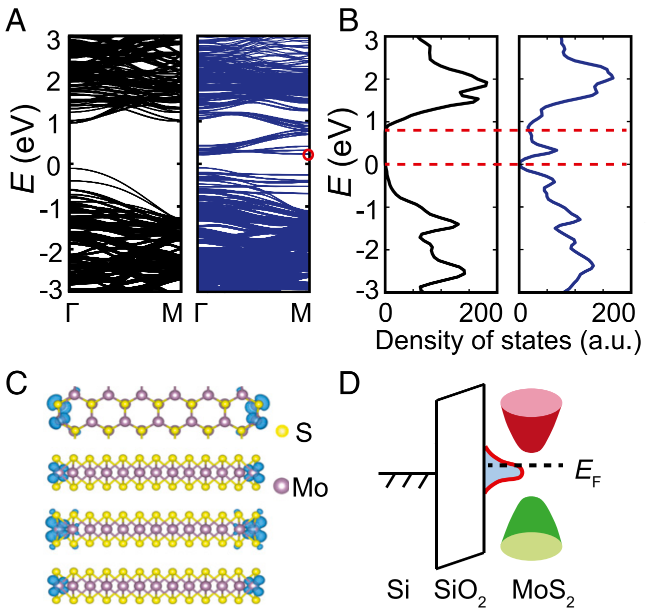

Fig. 4. DFT calculations of three-layer MoS_2 edge states. (*A*) Calculated band structures of the three-ML bulk MoS_2 (*Left*) and a 1.9-nm-wide MoS_2 nanoribbon with armchair edges (*Right*). (*B*) Total DOS of the same bulk (*Left*) and nanoribbon (*Right*) MoS_2. (*C*) Top view (*Uppermost Row*) and side view (*Lower Three Rows*) of the electron wave functions for selected orbitals, circled in *A*. The edge states are mainly localized at the boundary atoms. (*D*) Cartoon of edge and bulk band structures. As the Fermi level E_F moves upward, the edge states will be populated before the bulk states.

computed energy bands of an infinite 2D sheet and a nanoribbon with armchair edges of three-ML MoS_2. Compared with the bulk band structure, multiple bands appear within the bulk gap for the nanoribbon, reducing its energy gap from the bulk value of ~1.1 eV to ~0.3 eV, as also indicated by the density of states (DOS) plots in Fig. 4*B*. The charge density of additional electronic states at the *M* point of the Brillouin zone, circled in Fig. 4*A*, is well localized at boundary atoms in Fig. 4*C*, confirming that the additional bands in Fig. 4*A* are associated with the edge states. For a nanoribbon with zigzag edges, there are also edge states within the band gap, which connect the bulk conduction and valence bands as shown in Fig. S6 (18–20). For completeness, we have also included the DFT results of one-ML MoS_2 in Fig. S6, showing similar characteristics to the three-ML MoS_2. In reality, the edges in our devices may be a mixture of armchair and zigzag configurations, and the dangling bonds are usually terminated by foreign molecules from the environment. Nevertheless, the additional DOS inside the bulk band gap will be retained, leading to the topologically trivial edge states at the sample boundary (20, 22). As schematically illustrated in Fig. 4*D*, electrons will first populate the edge states with increasing V_{BG}. After these in-gap states are completely filled and g_{edge} is saturated, the further increase of V_{BG} will then raise the Fermi level E_F into the bulk conduction band, resulting in the upturn of g_{bulk}. Compared with the bulk bands, the edge bands are relatively flat, suggestive of higher effective mass and possibly lower mobility of the edge states. Consequently, once the bulk states participate in the transport at high gate voltages, the contribution of the edge states to the overall conductance becomes negligible. Such a physical picture nicely matches the evolution of local conductance maps deduced from the MIM data in Fig. 3*C*.

From the onset of bulk conduction at $V_{BG} = 5$ V to the saturation of MIM signals around $V_{BG} = 25$ V, pronounced spatial inhomogeneity with submicrometer length scale can be observed inside the MoS_2 flake. Both the strengths and spatial dimensions of the conductance fluctuations in this subthreshold regime are of critical importance for the device performance. We emphasize that the large variation of MIM signals cannot be accounted for by the surface roughness of the Al_2O_3 capping layer, as analyzed in Fig. S7. In Fig. 5*A*, the zoom-in MIM-Im images are displayed at $V_{BG} = -20$ V, 14 V, and 35 V, together with the corresponding line profiles in Fig. 5*B*. The variation of MIM signals at $V_{BG} =$ 14 V corresponds to local fluctuations of g_{bulk} from 5×10^{-8} S·sq to 2×10^{-7} S·sq in the four-ML region. Admittedly, the MIM-Im response (Fig. 2*C*) is also highly sensitive in this intermediate conductance range. Because the transistor is completely turned off for $V_{BG} = -20$ V (E_F below the bulk conduction band minimum E_C) and on for $V_{BG} = 35$ V (E_F well above E_C), as shown in Fig. 1*C*, it is reasonable to expect much weaker spatial conductance variations under these two conditions. On the other hand, electrical inhomogeneity is most significant when E_F intersects the spatially fluctuating E_C, as schematically shown in Fig. 5*C*. The MIM maps thus provide both quantitative measurements and direct visualization of the mesoscopic potential landscape in the sample (32), which is the combined effect from defects within the MoS_2 layer, charges inside the substrate and the capping layer, and impurities across the interface. The percolation network is vividly demonstrated in the subthreshold regime, which was only indirectly inferred from atomic scale or macroscale studies (18, 19). Note that a similar technique, the alternating current STM (40), can be applied to study the atomic-scale defects in MoS_2, which would provide complementary information to our MIM work.

In summary, we demonstrate the local conductance mapping of functional MoS_2 FETs by MIM. We find that, during the insulator-to-metal transition, electrons induced by the electrostatic field effect first populate the edge states before occupying the bulk of the 2D sheets, a scenario further corroborated by our first-principles calculations. The results unambiguously confirm that the contribution of edge states to the channel conductance is significant under the threshold voltage but negligible once the bulk becomes conductive. The magnitude and spatial dimensions of mesoscopic electrical inhomogeneity in the subthreshold regime are also visualized from the MIM data. The simultaneous macroscopic transport and mesoscopic imaging experiments on TMD FETs are critically important for both fundamental research and practical applications on these fascinating materials.

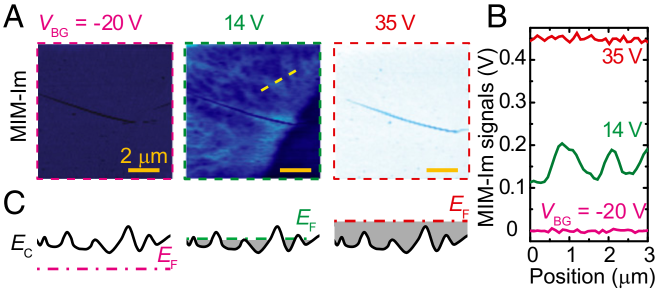

Fig. 5. Electrical inhomogeneity in the MoS_2 FET device. (*A*) Close-up MIM-Im images in the center of the flake at $V_{BG} = -20$ V, 14 V, and 35 V. (Scale bars, 2 μm.) (*B*) Line cuts along the orange dashed line in *A* at the three V_{BG} as in *A*. (*C*) Schematics of the relative positions between E_F and the spatially fluctuating E_C at the same V_{BG} as in *A* and *B*. The color coding (purple, green, and red) matches the solid circles in Fig. 1*C*.

Methods

Transport Measurements. Output and transfer characteristic curves are measured at the ambient condition with a semiconductor analyzer Keithley 4200.

MIM Measurements. The MIM in this work is based on an AFM platform (Park AFM XE-70). The customized shielded cantilevers are commercially available from PrimeNano Inc. FEA is performed using the commercial software COMSOL 4.4.

DFT Calculations. Density functional theory calculations are performed using the Vienna Ab Initio Simulation Package with the projector augmented wave method and Perdew−Burke−Ernzerhof exchange-correlation functional (41–43). For three-ML MoS$_2$, the interlayer van der Waals interactions are taken into account by Grimme's D2 correction (44). A plane wave cutoff of 400 eV and a **k**-point spacing smaller than 0.2 Å^{-1} along each periodic direction are used. A vacuum layer of larger than 15 Å is adopted to minimize the interaction between MoS$_2$ nanoribbon/sheet and its periodic images. Atomic structures are fully relaxed, with the force on each atom less than 0.01 eV/Å. The spin−orbit coupling (SOC) is included in the calculation of electronic properties, given a giant spin−orbit-induced spin splitting in MoS$_2$ layers (45). Denser **k** meshes and a Gaussian smearing of 0.1 eV are applied in the calculation of DOS. For an infinite sheet of one-ML and three-ML MoS$_2$, we construct supercells with a similar structure to corresponding armchair nanoribbons but without edges, which can be easily compared with the results of armchair nanoribbons.

ACKNOWLEDGMENTS. The MIM work (D.W., L.L., X.W., Z.C. and K.L.) was supported by the US Department of Energy (DOE), Office of Science, Basic Energy Sciences, under Early Career Award DE-SC0010308. D.W. acknowledges support from Welch Foundation Grant F-1814. W.L., M.N.Y., and D.A. acknowledge the support of Office of Naval Research under Contract N00014-1110190 and Nanomanufacturing Systems for Mobile Computing and Energy Technologies (NASCENT) Engineering Research Center under Cooperative Agreement EEC-1160494. Theoretical calculation (X.L. and Q.N.) was supported by China 973 Program (Projects 2013CB921900 and 2012CB921300), DOE (DE-FG03-02ER45958), and Welch Foundation (F-1255).

1. Wang QH, Kalantar-Zadeh K, Kis A, Coleman JN, Strano MS (2012) Electronics and optoelectronics of two-dimensional transition metal dichalcogenides. *Nat Nanotechnol* 7(11):699–712.
2. Radisavljevic B, Radenovic A, Brivio J, Giacometti V, Kis A (2011) Single-layer MoS$_2$ transistors. *Nat Nanotechnol* 6(3):147–150.
3. Zhang Y, Ye J, Matsuhashi Y, Iwasa Y (2012) Ambipolar MoS$_2$ thin flake transistors. *Nano Lett* 12(3):1136–1140.
4. Radisavljevic B, Kis A (2013) Mobility engineering and a metal-insulator transition in monolayer MoS$_2$. *Nat Mater* 12(9):815–820.
5. Baugher BWH, Churchill HOH, Yang Y, Jarillo-Herrero P (2013) Intrinsic electronic transport properties of high-quality monolayer and bilayer MoS$_2$. *Nano Lett* 13(9):4212–4216.
6. Chen X, et al. (2015) Probing the electron states and metal-insulator transition mechanisms in molybdenum disulphide vertical heterostructures. *Nat Commun* 6:6088.
7. Yuan HT, et al. (2013) Zeeman-type spin splitting controlled by an electric field. *Nat Phys* 9(9):563–569.
8. Wu SF, et al. (2013) Electrical tuning of valley magnetic moment through symmetry control in bilayer MoS2. *Nat Phys* 9(3):149–153.
9. Mak KF, McGill KL, Park J, McEuen PL (2014) Valleytronics. The valley Hall effect in MoS$_2$ transistors. *Science* 344(6191):1489–1492.
10. Yuan H, et al. (2014) Generation and electric control of spin−valley-coupled circular photogalvanic current in WSe$_2$. *Nat Nanotechnol* 9(10):851–857.
11. Zhang YJ, Oka T, Suzuki R, Ye JT, Iwasa Y (2014) Electrically switchable chiral light-emitting transistor. *Science* 344(6185):725–728.
12. Lee J, Mak KF, Shan J (2016) Electrical control of the valley Hall effect in bilayer MoS$_2$ transistors. *Nat Nanotechnol* 11(5):421–425.
13. Taniguchi K, Matsumoto A, Shimotani H, Takagi H (2012) Electric-field-induced superconductivity at 9.4 K in a layered transition metal disulphide MoS$_2$. *Appl Phys Lett* 101(10):042603.
14. Ye JT, et al. (2012) Superconducting dome in a gate-tuned band insulator. *Science* 338(6111):1193–1196.
15. Saito Y, et al. (2016) Superconductivity protected by spin−valley locking in ion-gated MoS$_2$. *Nat Phys* 12(2):144–149.
16. Ghatak S, Pal AN, Ghosh A (2011) Nature of electronic states in atomically thin MoS$_2$ field-effect transistors. *ACS Nano* 5(10):7707–7712.
17. Qiu H, et al. (2013) Hopping transport through defect-induced localized states in molybdenum disulphide. *Nat Commun* 4:2642.
18. Komsa HP, et al. (2012) Two-dimensional transition metal dichalcogenides under electron irradiation: Defect production and doping. *Phys Rev Lett* 109(3):035503.
19. Parkin WM, et al. (2016) Raman shifts in electron-irradiated monolayer MoS$_2$. *ACS Nano* 10(4):4134–4142.
20. Bollinger MV, et al. (2001) One-dimensional metallic edge states in MoS$_2$. *Phys Rev Lett* 87(19):196803.
21. Li Y, Zhou Z, Zhang S, Chen Z (2008) MoS$_2$ nanoribbons: High stability and unusual electronic and magnetic properties. *J Am Chem Soc* 130(49):16739–16744.
22. Xiao J, et al. (2015) Carrier mobility of MoS$_2$ nanoribbons with edge chemical modification. *Phys Chem Chem Phys* 17(10):6865–6873.
23. Zhang C, Johnson A, Hsu CL, Li LJ, Shih CK (2014) Direct imaging of band profile in single layer MoS$_2$ on graphite: Quasiparticle energy gap, metallic edge states, and edge band bending. *Nano Lett* 14(5):2443–2447.
24. Lai K, Kundhikanjana W, Kelly M, Shen ZX (2008) Modeling and characterization of a cantilever-based near-field scanning microwave impedance microscope. *Rev Sci Instrum* 79(6):063703.
25. Lai K, Kundhikanjana W, Kelly M, Shen ZX (2011) Nanoscale microwave microscopy using shielded cantilever probes. *Appl Nanosci* 1(1):13–18.
26. Yang YL, et al. (2012) Batch-fabricated cantilever probes with electrical shielding for nanoscale dielectric and conductivity imaging. *J Micromech Microeng* 22(11):115040.
27. Yuan H, et al. (2015) Influence of metal-MoS$_2$ interface on MoS$_2$ transistor performance: Comparison of Ag and Ti contacts. *ACS Appl Mater Interfaces* 7(2):1180–1187.
28. Chang H-Y, et al. (2016) Large-area monolayer MoS$_2$ for flexible low-power RF nanoelectronics in the GHz regime. *Adv Mater* 28(9):1818–1823.
29. Lai K, Ji MB, Leindecker N, Kelly MA, Shen ZX (2007) Atomic-force-microscope-compatible near-field scanning microwave microscope with separated excitation and sensing probes. *Rev Sci Instrum* 78(6):063702.
30. Lai K, et al. (2011) Imaging of Coulomb-driven quantum Hall edge states. *Phys Rev Lett* 107(17):176809.
31. Ma EY, et al. (2015) Unexpected edge conduction in mercury telluride quantum wells under broken time-reversal symmetry. *Nat Commun* 6:7252.
32. Ren Y, et al. (2015) Direct imaging of nanoscale conductance evolution in ion-gel-gated oxide transistors. *Nano Lett* 15(7):4730–4736.
33. Kaasbjerg K, Thygesen KS, Jacobsen KW (2012) Phonon-limited mobility in n-type single-layer MoS$_2$ from first principles. *Phys Rev B* 85(11):115317.
34. Splendiani A, et al. (2010) Emerging photoluminescence in monolayer MoS$_2$. *Nano Lett* 10(4):1271–1275.
35. Das S, Chen HY, Penumatcha AV, Appenzeller J (2013) High performance multilayer MoS$_2$ transistors with scandium contacts. *Nano Lett* 13(1):100–105.
36. Berweger S, et al. (2015) Microwave near-field imaging of two-dimensional semiconductors. *Nano Lett* 15(2):1122–1127.
37. Halperin BI (1982) Quantized Hall conductance, current-carrying edge states, and the existence of extended states in a two-dimensional disordered potential. *Phys Rev B* 25(4):2185–2190.
38. Kane CL, Mele EJ (2005) Z$_2$ topological order and the quantum spin Hall effect. *Phys Rev Lett* 95(14):146802.
39. Bernevig BA, Zhang SC (2006) Quantum spin Hall effect. *Phys Rev Lett* 96(10):106802.
40. Weiss PS, McCarty GS (2003) US Patent 6,597,194 B2.
41. Kresse G, Furthmüller J (1996) Efficient iterative schemes for ab initio total-energy calculations using a plane-wave basis set. *Phys Rev B Condens Matter* 54(16):11169–11186.
42. Perdew JP, Burke K, Ernzerhof M (1996) Generalized gradient approximation made simple. *Phys Rev Lett* 77(18):3865–3868.
43. Kresse G, Joubert D (1999) From ultrasoft pseudopotentials to the projector augmented-wave method. *Phys Rev B* 59(3):1758–1775.
44. Grimme S (2006) Semiempirical GGA-type density functional constructed with a long-range dispersion correction. *J Comput Chem* 27(15):1787–1799.
45. Zhu ZY, Cheng YC, Schwingenschlogl U (2011) Giant spin-orbit-induced spin splitting in two-dimensional transition-metal dichalcogenide semiconductors. *Phys Rev B* 84(15):153402.
46. Liu Y, et al. (2014) Mesoscale imperfections in MoS$_2$ atomic layers grown by a vapor transport technique. *Nano Lett* 14(8):4682–4686.
47. Molina-Sanchez A, Wirtz L (2011) Phonons in single-layer and few-layer MoS$_2$ and WS$_2$. *Phys Rev B* 84(15):155413.